3

Speckle Reduction in Echocardiography: Trends and Perceptions

Seán Finn, Martin Glavin and Edward Jones
National University of Ireland, Galway
Republic of Ireland

1. Introduction

Speckle is the fine-grained texture-like pattern seen in echocardiography, and indeed in all modalities of clinical ultrasound. The application of various image processing techniques to ultrasonography has been explored in the literature, and a common goal is the reduction or removal of the speckle component while preserving image structure. This assumes that speckle is a form of noise which is best removed; a view that is not always shared by those in clinical practice. This chapter presents a thorough overview of current trends in ultrasonic speckle reduction techniques, with an emphasis on echocardiography.

The phenomenon of speckle formation is described in Section 2 below. A review of the statistical methods used to model speckle is also presented in this chapter. Section 3 then details the main approaches for speckle reduction, covering the most recent of both compounding and post-acquisition techniques. Section 4 of this chapter presents a review and analysis of the methods of evaluation used to rate the performance of various speckle reduction approaches for clinical ultrasound. A particular focus is given to those which include consultation with practising clinicians in the field. The relationship between subjective clinical opinion and some objective image quality metrics on the quality of speckle filter echocardiographic video will be detailed. Details will be presented of a comprehensive evaluation methodology, which aims to combine clinical expertise and numerical assessment. Finally, Section 5 will conclude the chapter.

2. Speckle formation and statistics

While the term *ultrasound* can technically be used to refer to all acoustics of frequency greater than the upper threshold of human audibility ($f > 20$ kHz), clinical imaging is generally in the 1-20 MHz range (Rumack et al., 2004). Imaging is based on the transmission of acoustic pulses into the body, which interact with the tissue medium. Echoes are reflected by interfaces between tissue of differing acoustic properties, which are detected by a receiver. If the propagation velocity of sound waves in the imaged medium is known, the depth of interactions giving rise to the echoes can be determined. Characteristics of the returned signal (e.g. amplitude, phase) provide information on the interaction, and indicate the nature of the media involved. The amplitude of the reflected signal is used to produce ultrasound images, while the frequency shifts provide information on moving targets such as blood. Fig. 1 displays examples of clinical echocardiograms containing speckle.

The propagation speed in tissue varies with tissue type, temperature and pressure. Assuming constant temperature and pressure in the body, only the tissue type is considered (Quistgaard, 1997). The mean speed of sound propagation in human soft tissue is generally taken as 1540 m/s. Acoustic pulses transmitted into the body can experience:

Reflection: Also known a backscatter, reflection occurs when an acoustic pulse encounters an interface between tissues of differing acoustic impedances.

Refraction: When sound waves pass through an interface between media of different propagation speeds, a change in the direction of propagation occurs.

Absorption: Energy from the acoustic pulse is absorbed into the tissue, by conversion to thermal energy.

The acoustic impedance of a medium (Z) is the product of its density, ρ, and the speed of acoustic propagation in that medium, c ($Z = \rho c$).

The strength of reflection at an interface depends on the difference in acoustic impedance on each side of the boundary, as well as the size of the interface, its surface characteristics, and the angle of insonification. (Middleton & Kurtz, 2004; Rumack et al., 2004). The reflection coefficient at the interface is given in the same manner as the analogous case of electromagnetic propagation:

$$\Gamma = \frac{Z_2 - Z_1}{Z_2 + Z_1} \tag{1}$$

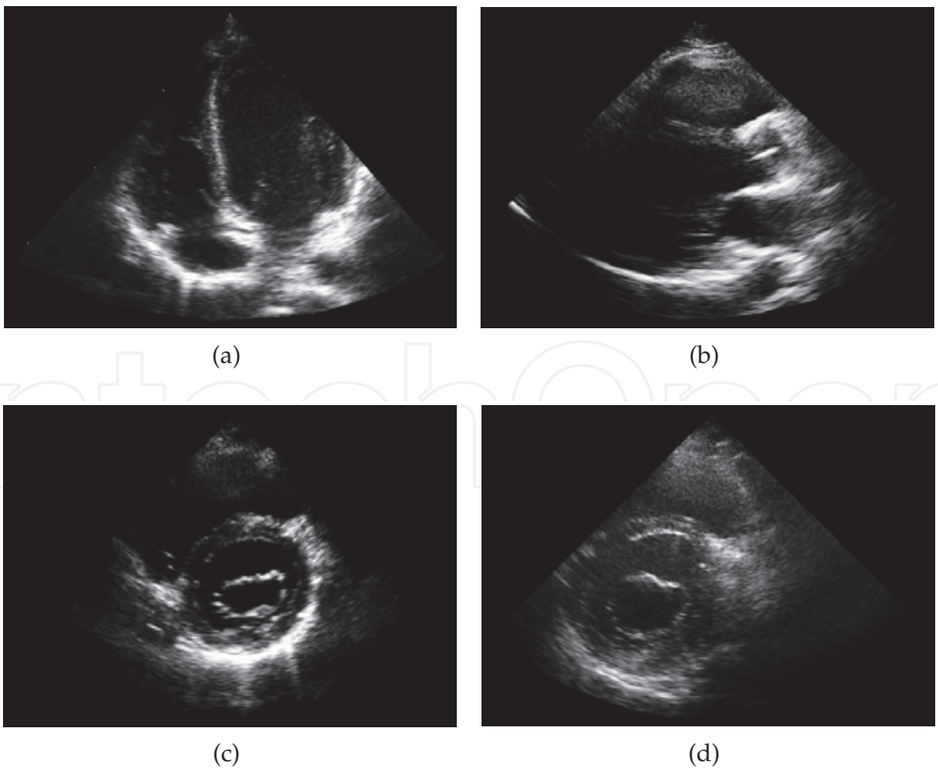

(a) (b) (c) (d)

Fig. 1. Clinical ultrasound images, used in speckle filter evaluation.

Depending on the nature of the interface, two types of reflection are observed: *Specular Reflection* occurs when the interface is large and smooth with respect to the ultrasound pulse wavelength, e.g. the diaphragm and a urine filled bladder (Rumack et al., 2004). Strong clear reflections are produced, in the same fashion as for a mirror. Detection of these echoes is highly dependent on the angle of insonification (Rumack et al., 2004). *Scattering* results from interfaces much smaller than the wavelength of the ultrasound pulse. A volume of small scattering interfaces such as blood cells or a non smooth organ surface produce echoes which are scattered in all directions. This collection of scatterers are said to act as a diffuse reflector. The constructive and destructive interference of these scattered echoes results in a granular artefact known as *speckle*. Refraction is governed by Snell's law:

$$\frac{\sin\theta_1}{\sin\theta_2} = \frac{c_1}{c_2} \tag{2}$$

where the quantities θ_1, θ_2, c_1, and c_2 are respectively the angles of incidence and refraction, and the corresponding speeds of propagation. Attenuation of the acoustic pulse is mainly due to absorption and scattering (Quistgaard, 1997), and can be modelled as: $A(x,t) = A(x,0)e^{-\alpha f 2x}$ (Thijssen, 2003). where $A(x,t)$ is the amplitude at depth x and time t, f is the frequency and α is the attenuation coefficient. Generally attenuation is quite severe: in (Quistgaard, 1997), a halving of intensity every 0.8 cm at 5 MHz operation is described.

The interference experienced by reflections from diffuse scatterers result in a granular pattern known as speckle. Speckle is common to all imaging systems using coherent waves for illumination, including laser and radar imagery. In echocardiography, speckle noise is prominent in all cross-sectional views (Massay et al., 1989), and its effect is far more significant than additive noise sources such as sensor noise (Zong et al., 1998).

The basic description of ultrasound speckle in the literature is based on the characterisation of laser speckle by Goodman (Goodman, 1975; 1976). This approach is extended to acoustic imagery by a number of authors (Burckhardt, 1978; Wagner et al., 1988; 1983). Burckhardt (Burckhardt, 1978) notes that despite its random appearance, speckle is essentially deterministic: scans under identical situations produce the same speckle pattern. This behaviour is in contrast to that of true stochastic processes such as electrical noise. There is no direct relationship between the imaged medium and the observed speckle pattern however. If the same object is imaged with different imaging parameters, the speckle pattern produced is quite different. Burckhardt thus concludes that the speckle pattern has only a tenuous relationship to the imaged medium, and is instead dependant on the parameters of the imaging system. The size of the speckle granules are of similar size to the resolution of the scanner, in both axial and lateral directions. Burckhardt justifies the treatment of pulsed acoustics as a coherent wave source in the situation where the each pulse contains a number of cycles of the carrier wave.

Each ultrasound pulse encloses a three dimensional volume which defines the smallest resolvable structure, which is known as the resolution cell. The nature of the speckle at an image location is determined by the number of diffuse scatterers which are present in the resolution cell at the relevant position in the imaged medium. If the number of scatterers is large and randomly positioned, the resulting pattern is known as fully formed (or fully developed) speckle. In this case the speckle pattern depends only on the imaging system.

Wagner *et al.* (Wagner et al., 1983) show that in the case of a mixture of diffuse and specular scattering, the speckle pattern is related to the underlying texture of the medium.

The randomly scattered echoes from the scatterers are summed within each resolution cell. These echoes are sinusoidal in nature. Expressed as phasors, the summation is described as a random walk of the real and imaginary components. In the case of fully developed speckle, and with uniformly distributed phase values between 0 and 2π, these components have a circular Gaussian distribution (Wagner et al., 1983):

$$p(a_r, a_i) = \frac{1}{2\pi\sigma^2} \exp\left(-\frac{a_r^2 + a_i^2}{2\sigma^2}\right) \tag{3}$$

where (a_r, a_i) are the real and imaginary components. The amplitude within each resolution cell, $A = \sqrt{a_r^2 + a_i^2}$, is then given by a Rayleigh distribution:

$$p(A) = \frac{A}{\psi} \exp\left(-\frac{A^2}{2\psi}\right), \quad A \geq 0 \tag{4}$$

The Rayleigh parameter ψ depends on the mean square scattering amplitude of the medium (Goodman, 1975). Burckhardt defined an SNR measure for the amplitude as $SNR_A = \bar{A}/\sigma_A$. i.e. the ratio of mean to standard deviation. It can be shown that $SNR_A = 1.91$ for the Rayleigh distribution of fully developed speckle. Burckhardt explores the statistics of image compounded from multiple individual scans, and demonstrates a method of simulating a theoretically maximally speckle free image from a known structure. Alternative distributions to Rayleigh have been proposed for situations not meeting the requirements of fully developed speckle, such as insufficient numbers of scatterers per resolution cell, or non random positioning. These include the Rician, Nakagami and *K* distributions (Shankar et al., 2001; Shankar, 1995; Smolíováí et al., 2004).

The number of scatterers required for fully formed speckle varies in the literature. Ten or greater is a common figure (Krissian et al., 2007; Lizzi et al., 1997; Thijssen, 2003), although it is stated in (Ng et al., 2006) that at least thirty scatterers should be present for the central limit theorem to hold. It has also been shown that neither the number of scatterers or their random positioning are required for fully developed speckle governed by Rayleigh statistics (Dantas et al., 2005): a sparse set of uniformly positioned equivalent scatters can also produce a fully formed speckle pattern.

3. Techniques for reducing speckle

The reduction of speckle while preserving image structure is a challenging image processing problem, due to the multiplicative-like behaviour of speckle. This can is evident from the relatively large volume of literature dedicated methods of reducing or eliminating speckle. The common justifications for the removal of speckle in these works are the general reduction in image quality due to the presence of speckle. However, the question of whether or not to remove speckle as noise in clinical imagery is an open one, and depends largely on the application. A number of specific negative effects of speckle, and benefits of its removal in clinical ultrasonography have been noted:

- Speckle introduces spurious 'false-fine' structures, which give the appearance of resolution beyond that of the imaging system (Dantas et al., 2005).
- Small grey level differences can be masked (Burckhardt, 1978), which can obscure tissue boundaries (Dantas & Costa, 2007; Dantas et al., 2005).
- Image contrast is reduced (Dantas & Costa, 2007; Zhang et al., 2007).
- Human interpretation of ultrasonography can be negatively impacted (Abd-Elmoniem et al., 2002; Zhang et al., 2007; Zong et al., 1998), introducing a degree of subjectivity (Dantas & Costa, 2007). The presence of speckle has been determined to be the cause of an eight-fold reduction in lesion detectability (Bamber & Daft, 1986). Reduction of echocardiographic speckle has been shown to positively affect subjective image quality and improve boundary definition (Massay et al., 1989).
- The effectiveness (speed and accuracy) of automated processing tasks is also reduced by speckle (Abd-Elmoniem et al., 2002; Yu & Acton, 2002; Zhang et al., 2007; Zong et al., 1998), such as edge detection, segmentation and registration.
- While speckle can be viewed as deterministic (Dantas et al., 2005), it does not contain information on the imaged structure in the fully developed speckle case.

Approaches to speckle reduction can be broadly grouped into compounding and postacquisition methods.

3.1 Compounding approaches

These techniques combine two or more images of the same area. The measurements from image structure will be partially correlated, while the speckle pattern will differ. Compounding these images (e.g. by averaging) results in an image with enhanced structure and a reduced speckle pattern. A number of different scanning methods can be used to produce the images to be compounded. Frequency compounding uses images with separate frequency ranges within the transducer bandwidth (Galloway et al., 1988; Gehlbach & Sommer, 1987; Magnin et al., 1982; Trahey, Allison, Smith & von Ramm, 1986). A common technique is spilt spectrum processing (SSP) (Bamber & Phelps, 1991; Newhouse et al., 1982; Stetson et al., 1997), in which the wideband RF signal is split into a number of subbands using bandpass filters. Envelope detection of these RF subbands yields amplitude data, which is combined to produce an image with enhanced structure and reduced speckle component. The recent method of Dantas and Costa (Dantas & Costa, 2007) is applied to the entire 2D RF image. This is in contrast to some SSP methods, which are applied to each 1D RF scan line individually. The RF image was decomposed into a number of orientation specific subbands by use of a bank of modified log Gabor filters. Each subband RF image was used to generate an amplitude image, and the final speckle reduced image was produced by compounding these amplitude images. The technique was tested by application to simulated images and comparison to maximally speckle free reference images generated using the method of Burckhardt (Burckhardt, 1978).

Other compounding approaches include spatial compounding, which combine multiple images from different scan directions (O'Donnell & Silverstein, 1988; Pai-Chi & O'Donnell, 1994; Trahey, Smith & von Ramm, 1986). Burckhardt (Burckhardt, 1978) showed that in order for these scans to be independent of each other (and so having uncorrelated speckle patterns), the transducer must be translated by approximately half its element width.

Temporal compounding (frame averaging) operates as the name suggests by combining scans performed over time. This approach suffers from a dependence on motion: in a still medium the speckle pattern will not change. Conversely, fast moving organs such as the heart may appear smeared with this method. Some modern ultrasound system are capable of performing spatial compounding by sweeping the scan beam over the medium, while the transducer is held statically (Jespersen et al., 2000). A recent transducer design makes use of a particular arrangement of receive elements to acquire multiple independent images simultaneously (Behar et al., 2003).

3.2 Postacquisition speckle reduction

Postacquisition methods operate on the image after it has been envelope detected, and have the advantage of not requiring a specific mode of scanning, or access to the RF data. Aa simulation study comparing postacquisition filters to spatial compounding reported better image improvement for filtering, in terms of speckle reduction and image quality (Adam et al., 2006). The number of postacquisition speckle reduction methods in the literature is large, and the selection detailed here are grouped according to their general approach.

3.2.1 Adaptive filters

Adaptive filters attempt to adjust the level of filtering at each image location. The Lee filter (Lee, 1980; 1981), Kuan filter (Kuan et al., 1987) and Frost filter (Frost et al., 1982) were proposed for the task of speckle removal in synthetic aperture radar (SAR), and assume a multiplicative model for speckle noise. Enhanced versions of the Lee and Frost filter were also proposed (Lopes et al., 1990). These are improved by the classification of image pixels into a number of classes, and filtering accordingly. The method of Bamber and Daft (Bamber & Daft, 1986) extended this adaptive approach to ultrasound images by varying the degree of smoothing according to a local estimate of the level of speckle.

Median filtering was extended to the case of speckle removal by Loupas *et al.* (Loupas et al., 1989). This approach replaced pixels with the weighted median of a dynamically sized window, and is known as the adaptive weighted median filter (AWMF). Region growing techniques such as (Chen et al., 2003; Huang et al., 2003; Karaman et al., 1995; Koo & Park, 1991) have been applied to ultrasonography. Pixels are grouped in these methods, according to similarity of intensity and connectivity. Spatial filtering is performed to extend these regions, and the challenge is the selection of appropriate similarity criteria.

A recently proposed method by Tay *et al.* (Tay et al., 2006a;b) used an iterative technique of speckle reduction by the removal of outliers. The locale around each pixel is examined, and local extrema are replaced with a local average. This process is repeated until no further outliers are found. Thus the filter reduces the local variance around each pixel, and is referred to by the authors as the "Squeeze Box" filter.

The non-local means filter of Coupé *et al.* (Coupé et al., 2009) estimates the true value of each pixel as the weighted sum of the windowed averages of within a search volume centred at the pixel of interest. This technique was adapted to speckled ultrasonography by incorporation of a multiplicative noise model by Bayesian estimation.

Massay *et al.* (Massay et al., 1989) proposed a method of speckle reduction using local statistics: the level of smoothing is determined by an estimate of local speckle level.

3.2.2 Diffusion filtering

Perona and Malik (Perona & Malik, 1990) introduced the first anisotropic diffusion method for additive noise. This is an iterative method of smoothing an image, similar in concept to heat diffusion.

A diffusion function is calculated at each iteration, with the aim of inhibiting smoothing across image edges and permitting it in homogeneous areas. Diffusion takes place according to the following Partial Differential Equation (PDE):

$$\frac{\partial I(x,y;t)}{\partial t} = \nabla \cdot \{c(|\nabla I_\sigma(x,y;t)|).\nabla I(x,y;t)\}, \quad I(x,y;0) = I_0(x,y) \tag{5}$$

where $I(x,y;t)$ is the image under diffusion, t is an artificial time dimension representing the progress of diffusion, I_0 is the observed image, ∇ and $\nabla \cdot ()$ are the gradient and divergence operators, and $|\cdot|$ represents magnitude. The diffusion function $c(\cdot)$ controls the level of diffusion at each image position. Smoothing is inhibited across image edges by choosing a monotonically decreasing function of gradient magnitude for $c(|\nabla I(x,y;t)|)$, such as $c(x) = e^{-(x/k)^2}$. Here k is an edge threshold, set to 90% of the absolute gradient histogram integral. A number of extensions to this method have been proposed, most notably that of Catté *et al.* (Catté et al., 1992), who regularised the calculation of $c(\cdot)$. This makes (5) mathematically well-posed, having a unique solution. While this method is capable of intra-region smoothing with edge preservation for images corrupted with additive noise, its effect on images corrupted with multiplicative noise is less than satisfactory (Yu & Acton, 2002).

To address the unsiutablility of Perona and Malik's diffusion for multiplicative speckled situations, Yu and Acton (Yu & Acton, 2002) proposed a diffusion function based on the coefficient of variation used in synthetic aperture radar:

$$\frac{\partial I(x,y,t)}{\partial t} = \nabla.[c(q).\nabla I(x,y,t)], \quad I(x,y,0) = I_0(x,y) \tag{6}$$

In contrast to (5), the diffusion function $c(.)$ is not a function of the gradient magnitude, but rather of the Instantaneous Coefficient of Variation (ICOV) q. The ICOV is based on the variation coefficient used in SAR filtering as a signal/edge discriminator, and is defined as:

$$q(x,y,t) = \sqrt{\frac{(0.5)\left(|\frac{\nabla I}{I}|\right)^2 - (0.25)^2\left(\frac{\nabla^2 I}{I}\right)^2}{[1+(0.25)\left(\frac{\nabla^2 I}{I}\right)]^2}} \tag{7}$$

where ∇^2 is the Laplacian operator. The diffusion function $c(.)$ used here is:

$$c\left[q(x,y,t), q_0(t)\right] = \left(1 + \frac{q^2(x,y,t) - q_0^2(t)}{q^2(x,y,t)(1+q_0^2(t))}\right)^{-1} \tag{8}$$

where q_0 is the 'speckle scale function', a diffusion threshold controlling the level of smoothing, equivalent to the noise variation coefficient C_n of the SAR filters.

The work of Aja-Fernandez and Alberola-Lopez (Aja-Fernandez & Alberola-Lopez, 2006) proposed a number of improvements to the SRAD technique, known as detail preserving anisotropic diffusion (DPAD). Noting that (8) is derived from the Lee filter, this is replaced with the following derived from the Kuan filter:

$$c\left[q(x,y,t),q_0(t)\right] = \frac{1+1/q^2(x,y,t)}{1+1/q_0^2(t)} \tag{9}$$

The second alteration concerns the calculation of the ICOV, showing that (7) is equivalent to the ratio of local standard deviation and mean estimators. In (7), these local estimators were calculated in using the four nearest neighbours of each pixel, while in DPAD a larger neighbourhood is used for more accurate estimates:

$$q(x,y,t) = \sqrt{\frac{\sigma_I^2(x,y,t)}{\bar{I}(x,y,t)^2}} = \sqrt{\frac{\frac{1}{|\eta_{x,y}|-1}\sum_{p\in\eta_{x,y}}\left(I_p-\bar{I}(x,y,t)\right)^2}{\bar{I}(x,y,t)^2}} \tag{10}$$

where $\eta_{x,y}$ is a square $Z \times Z$ neighbourhood, and $\bar{I}(x,y,t) = (1/|\eta_{x,y}|)\sum_{p\in\eta_{x,y}} I_p$. This is shown to be more accurate than the formulation of (7). The third contribution of (Aja-Fernandez & Alberola-Lopez, 2006) related to the estimation of $q_0(t)$, calculated as $median\{q(x,y;t)\}$. This approach requires less computation than the previously proposed method of (Yu & Acton, 2004), and produced similar results.

Tensor valued schemes, proposed by Weickert (Weickert, 1998; 1999), allow the strength of diffusion to vary directionally at each location. Denoted Coherence Enhancing Diffusion (CED), Weickert's method aims to enhance the enhance the smooth curves within an image, such as those often present in medical images. The structure tensor T is used to describe the image gradient:

$$T \quad = \nabla I \otimes \nabla I^T = \begin{pmatrix} I_x^2 & I_{xy} \\ I_{xy} & I_y^2 \end{pmatrix} \tag{11}$$

where I_x, I_y are the x and y gradients of the image: $\nabla I = (I_x, I_y)$. To make the gradient description robust to small noise fluctuations, local averaging of the observed image is performed as $I_\sigma = K_\sigma * I$, where $*$ represents convolution, and K_σ is a Gaussian kernel of variance σ^2. The gradient ∇I_σ represents only information from image details larger than $O(\sigma)$. Thus σ is referred to as the *noise scale*. The structure tensor is formed using a second level of Gaussian smoothing:

$$T_\rho = K_\rho * (\nabla I_\sigma \nabla I_\sigma^T) = \begin{pmatrix} T_{11} & T_{12} \\ T_{21} & T_{22} \end{pmatrix} \tag{12}$$

The values of T_ρ then represent image information from a neighbourhood defined by ρ, the *integration scale*. While the structure tensor is simply another representation of the image gradient ∇I, and contains no more information than ∇I, it has the advantage of allowing local averaging as in (12) without cancellation.

The eigenvectors of T_ρ are denoted by $(\vec{\omega}_1, \vec{\omega}_2)$, and the corresponding eigenvalues by (μ_1, μ_2). If the eigenvalues are ordered so that $\mu_1 \geq \mu_2$, then $(\vec{\omega}_1, \vec{\omega}_2)$ give the directions of maximum and minimum local variation, respectively. These are the directions normal and tangent to the local image gradient, the gradient and contour directions. The corresponding eigenvalues give the strength of the gradient in these directions, and also provide information on the local coherence or anisotropy. A measure of local coherence is defined as $\kappa = (\mu_1 - \mu_2)^2$ (Weickert, 1999). The CED diffusion process is described by the PDE:

$$\frac{\delta I(x,y,t)}{\delta t} = \nabla.(D\nabla I(x,y,t)) \tag{13}$$

where D is the diffusion matrix, constructed with the same eigenvectors as T_ρ ($\vec{e}_1 = \vec{\omega}_1, \vec{e}_2 = \vec{\omega}_2$) and eigenvalues (λ_1, λ_2) given by:

$$\lambda_1 \quad = \quad c_1, \quad \lambda_2 \quad = \begin{cases} c_1, & \text{if } \mu_1 = \mu_2 \\ c_1 + (1 - c_1)\exp\left(\frac{-c_2}{\kappa}\right), & \text{otherwise} \end{cases} \tag{14}$$

where c_1 and c_2 are parameters constrained by $0 < c_1 \ll 1$ and $c_2 > 0$.

The nonlinear coherent diffusion (NCD) method of Abd-Elmoniem *et al.* (Abd-Elmoniem et al., 2002) is a tensor valued anisotropic diffusion scheme for the removal of speckle. The eigenvalues of the diffusion tensor define the directional strength of diffusion at each image location, and these are chosen to reflect an estimate of the strength of speckle at that location. Image regions closely resembling fully developed speckle are mean filtered, while those dissimilar remain unaltered. Similar to the CED method, this approach uses a tensor-valued diffusion function, calculated as a component-wise convolution of a Gaussian kernel with the structure tensor:

$$J_\rho \quad = K_\rho * (\nabla I \, \nabla I^T) = \begin{pmatrix} K_\rho * I_x^2 & K_\rho * I_{xy} \\ K_\rho * I_{xy} & K_\rho * I_y^2 \end{pmatrix} \tag{15}$$

Here, the initial stage of smoothing performed in (12) is not used. As in the CED method, ρ is integration scale, the window size over which the orientation information is averaged. The PDE (13) again describes the diffusion, using a diffusion tensor constructed so as to have the same eigenvectors as J_ρ, but with eigenvalues λ_1, λ_2 defined as:

$$\lambda_1 \quad = \quad \begin{cases} \alpha\left(1 - \frac{\kappa}{s^2}\right), & \text{if } \kappa \leq s^2 \\ 0, & \text{otherwise} \end{cases}, \quad \lambda_2 \quad = \quad \alpha \tag{16}$$

where α is a parameter determining the level of smoothing in regions of fully developed speckle, and s^2 is a heuristically chosen 'stopping level'.

The orientated SRAD (OSRAD) proposed by Krissian *et al.* (Krissian et al., 2007) extended the SRAD method to a tensor diffusion scheme, so diffusion can vary with direction to speckle adaptive diffusion filtering. The improvements of the DPAD method are also used in this method, such as the use of a larger window to estimate $q(x, y; t)$, and the median estimation of $q_0(t)$. The OSRAD diffusion function $c(q)$ is based on the Kuan *et al.* filter, as in (9). It was shown that the local directional variance is related to the local geometry of the image.

This method can be implemented by the use of the structure tensor, as in (Weickert, 1999) and (Abd-Elmoniem et al., 2002), or by using the Hessian matrix as in (Krissian, 2002). In the 2-D case, $(\vec{\omega}_1, \vec{\omega}_2)$ are the eigenvectors of T_ρ from (12), and are used as the basis of the diffusion matrix, D. The eigenvalues of D, which determine the strength of diffusion in the gradient and curvature directions, are given as:

$$\lambda_1 \quad = c_{srad} \quad , \quad \lambda_2 \quad = c_{tang} \tag{17}$$

Where c_{srad} is the SRAD diffusion ($c(q)$), and c_{tang} is a constant. Diffusion is then performed as per (13).

3.2.3 Multiscale methods

Multiscale methods are common in image processing, and both the wavelet and pyramid (Burt & Adelson, 1983) transforms have been employed in the reduction of speckle. The well-known wavelet transform isolates local frequency subbands using a quadrature mirror pair of filters. The the pyramid transform does not require quadrature filters. More details on this method can be found in (Adelson et al., 1984).

Wavelet techniques can be grouped into those which operate by thresholding, Bayesian estimation, or correlation between coefficients. Many techniques use the soft thresholding approach of Donoho (Donoho, 1995), of which some of the first adoptions for speckle were proposed by (Guo et al., 1994) and (Moulin, 1993). These methods use a logarithmic transformation to allow treatment of the speckle as additive. The thresholding method of (Hao et al., 1999) operates on the output of the AWMF filter. The difference image between the AMWF output and the original image contains the high frequency information removed by the AWMF. Both images have speckle removed by soft thresholding in the wavelet domain, and after reconstruction the two images are summed together.

Using a multiplicative model for a speckled image, the method of Zong *et al.* (Zong et al., 1998) applies logarithmic and wavelet transforms as:

$$\begin{aligned} I(i,j) &= R(i,j)n(i,j) \\ I^l(i,j) &= R^l(i,j) + n^l(i,j) \\ W[I(i,j)] &= \{(W_k^d[I(i,j)])_{1\le k\le J}^{d=1,2}, S_K[I(i,j)]\} \end{aligned} \tag{18}$$

where R and n are the speckle free and speckle noise components, (i,j) are the pixel indecies, and $I^l = log(I)$. Here $n^l(i,j)$ is approximated as additive white noise. The K-level discrete Dyadic Wavelet Transform (DWT) of (Mallat & Zhong, 1992) generates $W_k^d\{I(i,j)\}$, the set of wavelet coefficients at scale 2^k (level k) and spatial orientation d ($d = 1$ for horizontal and $d = 2$ for vertical). The approximation coefficients at the coarsest scale K are denoted by $S_K\{I(i,j)\}$. Soft thresholding is applied to the finer scales (levels one and two), with coefficient dependent thresholds.

A nonlinear function is applied to the other, coarser, scales. This incorporates hard thresholding and a nonlinear contrast enhancement term:

$$E(v) = \begin{cases} 0, & \text{if} \quad |v| < T_1 \\ sign(v)T_2 + \bar{u}, & \text{if} \quad T_2 \leq |v| \leq T_3 \\ 1, & \text{otherwise} \end{cases} \tag{19}$$

where $v \in [-1, 1]$ represents each wavelet coefficient, and the three thresholds are related as $0 \leq T_1 \leq T_2 \leq T_3 \leq 1$. The value of $\bar{u}$ is determined according to $\bar{u} = a(T_3 - T_2)\{f[c(u-b)] - f[-c(u+b)]\}$. The sigmoid function is represented by f, and

$$u = \frac{sign(v)(|v| - T_2)}{T_3 - T_2}, \quad a = \frac{1}{f[c(1-b)] - f[-c(1+b)]} \tag{20}$$

Thus the operator $E(v)$ is dependant on five parameters: b, c, T_1, T_2, T_3.

Noise removal in the wavelet domain is also performed using Bayesian denoising techniques, which model the distributions of the wavelet coefficients. This a priori information is used to infer the noise free coefficients. Gupta *et al.* (Gupta et al., 2005) modelled the wavelet coefficients of the underlying speckle free image using a generalised Laplacian distribution, simultaneously removing speckle and performing compression using a quantisation function. This function adapts to the estimated level of speckle.

Achim *et al.* (Achim et al., 2001) modelled the wavelet coefficients of $I^l(i,j)$ as the convolution of a symmetric α stable (SαS) distribution (as $R(i,j)$), and a zero mean Gaussian distribution for $n(i,j)$. The variance of the Gaussian noise is estimated using the median absolute deviation (MAD) method, while the parameters of the SαS distribution are estimated by least squares fitting of the observed density function spectrum to the empirical characteristic function. After estimation of the parameters of the statistical model, a shrinkage function is found by numerical calculation of the maximum a posteriori (MAP) estimation curve. The wavelet coefficients are modified by the shrinkage function, and the inverse wavelet transform produces the denoised image.

The technique of Rabani *et al.* (Rabbani et al., 2008) models the distribution of the noise free wavelet coefficients using a local mixture of either Gaussian or Laplacian distributions. The speckle noise is assumed to be either Gaussian or Rayleigh in nature. For all combinations of local mixture distributions and speckle noise distributions, both the MAP and minimum mean squared error (MMSE) estimators are derived analytically. A recently proposed method by Fu *et al.* (Fu et al., 2010) accomplishes bivariate shrinkage of the wavelet coefficients. This approach models the joint density of the coefficients in each scale with their parents in the next coarser scale.

The third type of wavelet noise removal uses the correlation of useful wavelet coefficients across scales (Pižurica et al., 2003). This technique does not rely on a model for the image noise, but rather locates the signals of interest based on their interscale persistence. This initial classification step is followed by empirical estimates of the signal and noise probability density functions (PDFs). These are used to define a shrinkage map which suppress those wavelet coefficients resulting from noise.

The NMWD method (Yue et al., 2006) aims to combine wavelet analysis with anisotropic diffusion. Wavelet based signal/noise discrimination is employed to overcome the

shortcomings of the image gradient (as used in the PMAD, CED and NCD methods) for discrimination in speckled images. The gradient cannot always precisely separate the image and noise in ultrasound images, as variations due to speckle noise may be larger than those corresponding to underlying image (Yue et al., 2006). The image is decomposed using the DWT of Mallat and Zhong, as in the Zong *et al.* method. The modulus of the wavelet coefficients at each scale is defined as:

$$M_k\{I(i,j)\} = \sqrt{\sum_{d=1}^{2} |W_k^d\{I(i,j)\}|^2_{k=1,2,..,K}} \tag{21}$$

The normalised wavelet modulus was found to be large in edge-related regions and small for noise and texture, and so is used for signal/noise discrimination in this method. For amplitude images the wavelet modulus is normalised by:

$$\tilde{M}_k I = \frac{M_k\{I(i,j)\}}{\mu_Z}, \quad k = 1, 2, .., K \tag{22}$$

Here μ_Z is a local mean calculated using a widow size $Z \times Z$. The histogram of $\tilde{M}_k I$ is modelled as a Rayleigh mixture distribution, composed of the sum of edge and noise pixels as:

$$\tilde{M}_k I \simeq n_k p_{n,k}(x, \lambda_n) + (1 - n_k) p_{e,k}(x, \lambda_e) \tag{23}$$

where $p_{n,k}$ is a Rayleigh distribution with parameter λ_n, representing the noise pixels. Similarly, $p_{e,k}$ are the edge pixels, Rayleigh distributed with parameter λ_e. The proportion of the mixture distribution resulting from noise-related values is given as n_k. The parameters of the normalised modulus distribution ($\sigma_{n,k}$, $\sigma_{e,k}$ and n_k) are estimated using the Expectation-Maximisation (EM) method (Dempster et al., 1977). These parameters are used to determine the strength of n anisotropic diffusion process. After diffusion, the wavelet coefficients are used the synthesize the speckle reduced image. This process is repeated for a number of iterations.

As well as wavelet based methods, multiresolution pyramid methods of speckle reduction have been proposed. The approach of Aiazzi *et al.* (Aiazzi et al., 1998) extends the approach of the Kuan filter to process each layer in the multiscale pyramid decomposition. Sattar *et al.* (Sattar et al., 1997) presented a method which both reduces speckle and enhances image edges. Multiscale decomposition is performed using a pyramid transform. An edge detector is applied to the lowpass image, the output of which determines the coefficients from the high pass image which are included in reconstruction. The success of this method is therefore dependant on accurate operation of the edge detector, and a number of different techniques are tested.

The approach of Zhang *et al.* (Zhang et al., 2007) combines the approaches of multiscale analysis and anisotropic diffusion, and so is similar in approach to the NMWD method above.

4. Evaluation of speckle reduction

As shown above, a large variety of speckle reduction filters have been proposed. Evaluating the relative performance of these filters has been performed by a number of different methods.

The majority of the papers proposing these filters contain a comparison of the proposed method with some others from the literature. Common techniques for evaluating relative performance are quantitative image quality metrics, and qualitative inspection, often by the authors themselves. Test data for evaluation includes clinical and phantom images, as well as simulated ultrasound which allows evaluation of filtering relative to an ideal speckle free reference. A select number of independent reviews have also been published, which vary in the nature and depth of the investigation performed.

Thakur and Anand (Thakur & Anand, 2005) compared the suitability of a number of different wavelets for the reduction of speckle in ultrasound imagery. Adam *et al.* (Adam et al., 2006) looked at the effect of a combination of spatial compounding and postacquisition filtering. Different methods of compounding these images were evaluated in this work, in combination with a number of postacquisition filters. These were applied to simulated kidney images generated using the Field II software package (Jensen, 1996). It was shown that postacquisition filtering improved the images to a greater degree than compounding alone, and that the SRAD filter was the better of the two considered. A recent comparison by Mateo and Fernández-Caballero (Mateo & Fernández-Caballero, 2009) evaluated median filtering, the AWMF filter, two low-pass filters, and a simple wavelet filter. Lowpass filtering with the Butterworth filter was deemed by the authors to be the best of the methods considered. A comprehensive comparison of a large number of speckle reduction filters for application to clinical carotid ultrasonography was presented by Loizou *et al.* (Loizou et al., 2005). Evaluation was performed both by automated analysis, and also using classification by experts. In both cases, the focus was on the diagnosis of atherosclerosis (thickened artery walls due to plaque deposit). A set of clinical images from patients deemed to be at risk of this condition was used in filter evaluation, and these were divided into a symptomatic set (from patients who have displayed symptoms of this condition, such as stroke incidents), and an symptomatic set. For the test by automated analysis, 440 images were used, divided equally between the two sets. Automated analysis proceeded by calculating a large number (56) of texture features for each filtered image. The level of separability between the symptomatic and symptomatic sets was then analysed using a number of approaches, using a distance metric an the statistical Wilcoxon rank sum test. A set of image quality metrics were also applied, comparing the filtered image to the unfiltered version in each case. The expert test was performed with 100 images, split evenly between symptomatic and symptomatic groups. The filtered and unfiltered images were shown to two experts at random, and each expert rates the quality of the image on a scale of one to five. Only one method (the Geometric filter) was seen to improve the image quality as perceived by both experts across the entire dataset. A difference in the evaluations between the experts was noted, although this was not investigated statistically. The authors accounted for this by reference to the differing clinical specialities of the experts.

The present author conducted and reported on a study which compared clinical and computational evaluation of speckle filtering in echocardiographic images (Finn et al., 2009). Subjective visual assessment was performed by a group of six clinical experts, all of whom are experienced cardiac physicians or technicians. The majority of the evaluation strategies described in the literature review of the previous chapter report results of visual inspection by the authors themselves, rather than the opinion of clinical experts (exception include (Loizou et al., 2005; Zong et al., 1998)). The basic qualities which are generally held to

constitute favourable speckle filtering (homogeneous variance reduction, mean intensity preservation and edge preservation) can be readily determined visually, and do not require clinical expertise or training. However, the assessment of clinical images for diagnostic purposes does require such training and expertise. This study explored the clinical opinion of the quality of speckle filtered echocardiographic images, as judged by experts in the field. A large set of speckle filtered echocardiographic videos were produced by application of a number of speckle reduction filters: The SRAD filter (Yu & Acton, 2002), the NCD filter (Abd-Elmoniem et al., 2002), and the GLM filter proposed by Pižurica *et al.*. Example echocardiographic images processed by these filters are displayed in Fig. 2. A total set of forty eight filtered videos were produced in this fashion, showing differing levels of speckle reduction and image characteristics.

The clinical experts assessed subjective video quality in three criteria, chosen based on the opinion of a senior clinical expert of important clinical factors:

Speckle Level The expert's assessment of the level of speckle in each video.

Detail Clarity Quantifies the subjective resolvability of diagnostically important details.

Overall Quality This quantifies the overall quality of the video, including any other clinical considerations not covered by the other criteria.

A large set of quantitative image quality metrics, commonly used in the literature for evaluation of speckle reduction, were also applied. Statistical analysis was performed in order to determine:

1. If there were any significant differences between the expert scores
2. If there were any statistically significant relationships between the three scoring categories for each expert.

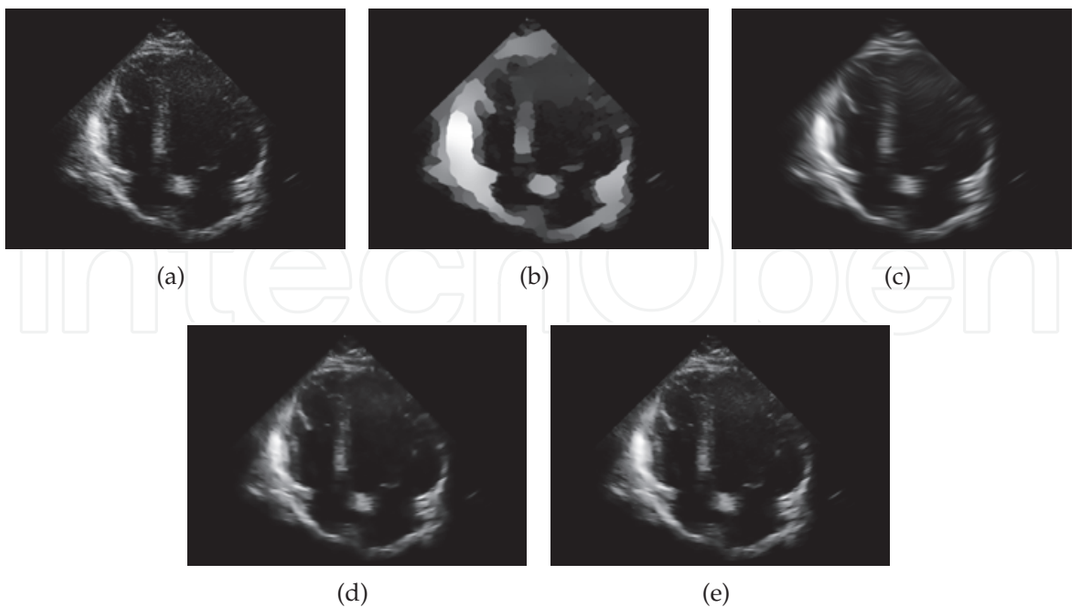

Fig. 2. Example frame from an echocardiographic video, from the long axis view. (a) Unfiltered, (b) SRAD, (c) NCD, (d) GLM, (e) NMWD.

3. If there were significant relationships between the subjective expert scores and the image quality metrics.

The expert scores are an ordinal categorical data set, and so the non-parametric Kruskal-Wallis test (Kruskal & Wallis, 1953) was used to investigate inter-expert differences. For the second and third analyses above, correlations were quantified using Spearman's rank correlation coefficient (ρ) (Spearman, 1904). All tests were performed using the SPSS software package, and the level of significance was chosen as 1% ($p = 0.01$) throughout.

Filtering resulted in a reduction in perceived Speckle Level in almost two thirds of cases. However, the aggregate Overall Quality and Detail Clarity scores were negative in over half of cases, indicating that the experts did not view speckle reduction as beneficial for manual analysis. This is in general agreement with the results of Loizou *et al.* (Loizou et al., 2005). The results of Dantas and Costa (Dantas & Costa, 2007) appear to be relevant: while speckle reduction does not necessarily lead to a loss of clarity, it does remove 'false-fine' structures (spurious fine detail, beyond the scanning resolution). While these details do not represent tissue structure, its removal can lead to a perceived reduction in sharpness. The assessment of the experts here was not universally negative however.

The Kruskal-Wallis test resulted in no no statistically significant differences between the experts in the Overall Quality scores at a 1% level of significance, but that a significant difference exists between experts in both the Speckle Level and Detail Clarity scores. For all of the experts, the relationship between Overall Quality and Detail Clarity is strongly positive and statistically significant. The ρ values for the relationship between Overall Quality and Speckle Level show positive relationships in all cases, but is only significant at the 1% level for four of the six experts. The relationship between the Detail Clarity and Speckle Level scores again indicate a positive relationship, and are significant for all but one of the experts.

The relationship between the expert scores and the objective image quality metrics is shown in Table 1 to be significant for three metrics:

Pratt's Figure of Merit (FoM) (Pratt, 1977) measures edge pixel displacement between each filtered image I_{filt} and the original image I_{orig}:

$$FoM(I_{filt}, I_{orig}) = \frac{1}{max(N_{filt}, N_{orig})} \sum_{i=1}^{\hat{N}} \frac{1}{1 + d_i^2 \alpha} \tag{24}$$

where N_{filt} and N_{orig} are the number edge pixels in edge maps of I_{filt} and I_{orig}. Parameter α is set to a constant $\frac{1}{9}$ (Yu & Acton, 2002), and d_i is the Euclidean distance between the i^{th} detected edge pixel and the nearest ideal edge pixel. The FoM metric measures how well the edges are preserved through out the filtering process. This metric is shown to have a significant relationship with the Overall Quality expert score at the 1% significance level.

Mean Squared Error (MSE) The MSE measures the average absolute difference between two the original and filtered images (average intensity change due to filtering):

$$MSE(I_{filt}, I_{orig}) = \frac{1}{XY} \sum_{i=1}^{Y} \sum_{j=1}^{X} (I_{filt}(i,j) - I_{orig}(i,j))^2 \tag{25}$$

where both images are of size $X \times Y$. This metric is shown to have a significant inverse relationship with the Speckle Level expert score at the 1% significance level.

Edge Region MSE This is the same as the MSE above, but only pixels in the vicinity of image edges are considered.

This metric is shown to have a significant relationship with the Detail Clarity expert score at the 1% significance level.

	Expert 1	Expert 2	Expert 3	Expert 4	Expert 5	Expert 6
Overall Quality / FOM	ρ=0.74 p=176.5×10^{-11}	ρ=0.59 p=123.0×10^{-7}	ρ=0.53 p=124.1×10^{-6}	ρ=0.72 p=607.0×10^{-11}	ρ=0.55 p=452.7×10^{-7}	ρ=0.82 p=992.7×10^{-15}
Detail Clarity / Edge Region MSE	ρ=-0.67 p=164.0×10^{-9}	ρ=-0.62 p=240.0×10^{-8}	ρ=-0.49 p=402.0×10^{-6}	ρ=-0.76 p=346.8×10^{-12}	ρ=-0.49 p=332.9×10^{-6}	ρ=-0.83 p=205.6×10^{-15}
Speckle Level / MSE	ρ=-0.69 p=531.1×10^{-10}	ρ=-0.47 p=726.0×10^{-6}	ρ=-0.85 p=306.8×10^{-16}	ρ=-0.47 p=710.1×10^{-6}	ρ=-0.64 p=992.1×10^{-9}	ρ=-0.87 p=214.3×10^{-17}

Table 1. Intra-expert association between scoring categories and metrics, using Spearmans correlation (ρ), with significance.

Having established relationships between objective image quality metrics and subjective expert opinion, the present author recently conducted a comprehensive review of speckle filtering methods as applied to echocardiography (Finn et al., 2010). A comprehensive evaluation of a wide range of techniques was performed, taking into account both clinical and simulated ultrasound images, and also the computational requirements of each method. Fifteen recent filtering approaches, including anisotropic diffusion, wavelet denoising and local statistics, were evaluated. These are summarised in Table 2.

Method	Type	Refrences	Abbreviation
Perona and Malik Diffusion	AD	Perona & Malik (1990)	PMAD
Speckle Reducing Anisotropic Diffusion	AD	Yu & Acton (2002)	SRAD
Detail Preserving Anisotropic Diffusion	AD	Aja-Fernandez & Alberola-Lopez (2006)	DPAD
Coherence Enhancing Diffusion	AD	Weickert (1999)	CED
Nonlinear Coherent Diffusion	AD	Abd-Elmoniem et al. (2002)	NCD
Oriented Speckle Reducing Anisotropic Diffusion	AD	Krissian et al. (2007)	OSRAD
Zong *et al.* Filter	W	Zong et al. (1998)	Zong
Generalized Likelihood Method	W	Pižurica et al. (2003)	GLM
Nonlinear Multiscale Wavelet Diffusion	W	Yue et al. (2006)	NMWD
Lee Filter	SAR	Lee (1980)	Lee
Frost *et al.* Filter	SAR	Frost et al. (1982)	Frost
Kuan *et al.* Filter	SAR	Kuan et al. (1987)	Kuan
Enhanced Lee Filter	SAR	Lopes et al. (1990)	EnhLee
Enhanced Frost *et al.* Filter	SAR	Lopes et al. (1990)	EnhFrost
Geometric Filter	-	Crimmins (1985)	Geo

Table 2. Despeckle Filter Summary. *AD* = Anisotropic Diffusion, *W* = Wavelet.

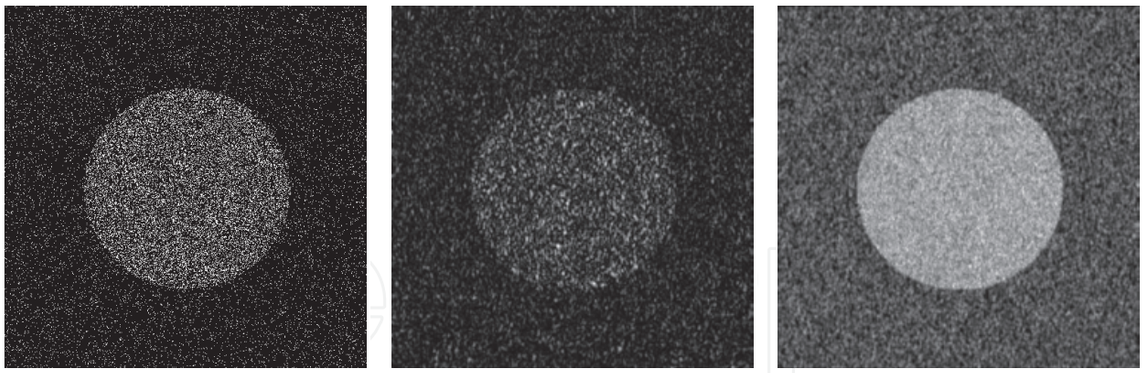

(a) (b) (c)

Fig. 3. Example simulated ultrasound image. (a) Echomap, (b) Speckled amplitude image, (c) Speckle free MW image.

Various approaches of varying simplicity have been employed in the literature to produce simulated images (Achim et al., 2001; Sattar et al., 1997; Yu & Acton, 2002). Ultrasound imaging can be treated as a linear process (Jensen, 1991; Ng et al., 2006), i.e. the filtering of an echogenicity map with a point spread function (PSF). An axially-varying PSF was used in (Ng et al., 2007), approximated as piecewise constant, similar to (Michailovich & Adam, 2005). This approach was also employed here, with PSFs at various depths generated using the Field II simulation software (Jensen, 1996) and demodulated to baseband.

While the PSF models the imaging system, the imaged medium is modelled as an echogenicity map $h(x, y)$ composed of complex point scatterers, similar to (Dantas & Costa, 2007). Scatterers are positioned randomly within regions of varying density. The phase values of the scatterers follows a uniform distribution, varying from $0 \rightarrow 2\pi$ rad, while scatterer magnitude follows a Gaussian distribution with unity mean and $\sigma = 0.1$. Fig. 3(a) shows an example of an echomap with two regions of differing scatterer densities, with density values of 40% and 10%. Echogenicity maps are filtered to generate a simulated image as $RF(x, y) = h(x, y) * p(x, y), I(x, y) = |RF(x, y)|$. where p is the analytic form of the PSF function at the correct depth, and $*$ denotes convolution. Examples of the granular speckle pattern produced can be seen in Fig. 3(b).

The Maximum Writing (MW) technique (Burckhardt, 1978) is used to generate a maximally speckle free version of each of the twenty simulated images. The above convolution is performed multiple times, randomly varying scatterer phase. This produces a series of images with the same structure but differing speckle patterns, the maximum of which is the speckle free image: $I_{MW} = \max\{|p(x, y) * (|h(x, y)| \exp[\phi_n])|\}$ (ϕ_n is the phase of the n^{th} set of scatterers generated). In practice, this technique is applied until the contribution of the n^{th} amplitude image is smaller than 0.1% of average image brightness, similar to the approach of (Dantas & Costa, 2007). Fig. 3(c) displays the MW output. A total of twenty simulated images are used in speckle filter evaluation. Fig. 4 displays typical results of filter application to the simulated images.

The output of the local statistics filters vary in the speckle suppression level: the Lee, Frost and enhanced Frost remove most of the speckle pattern with some blurring. The Kuan and

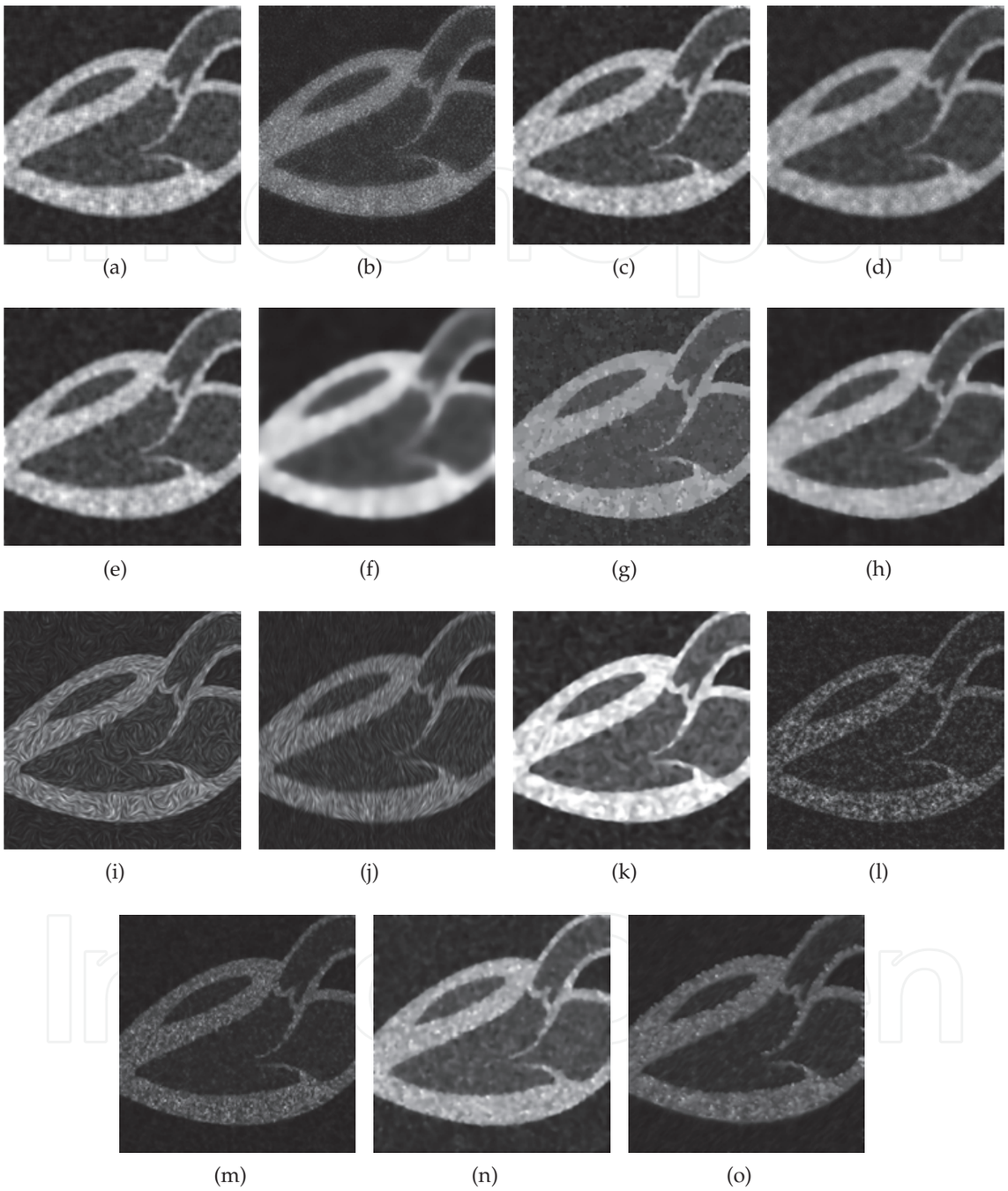

Fig. 4. Sample speckle filter output for a simulated image. (a) Lee, (b) Kuan, (c) Frost, (d) EnhLee, (e) EnhFrost, (f) PMAD, (g) SRAD, (h) DPAD, (i) CED, (j) NCD, (k) OSRAD, (l) Zong, (m) GLM, (n) NMWD, (o) Geo.

ehhanced Lee filter remove considerably less of the speckle pattern. The anisotropic diffusion filters also exhibit a range of output quality. The PMAD filter required many iterations to remove speckle, resulting in a blurred output. The SRAD and DPAD filters both display strong speckle suppression. Due to a larger window size, the DPAD filter remove more of the speckle, producing images which are more uniform. The CED method and the NCD filter both display artefacts, introduced by the enhancement of image contours (including those of the speckle texture). This effect is more pronounced for the NCD filter. The OSRAD filter displays a strong degree of speckle suppression, and preserves the image borders. The Zong and GLM filter outputs both show a degree of speckle remaining. The NMWD filter is seen to produce output with most of the speckle pattern removed. Finally, the Geometric filters output displays a good level of speckle reduction, however some of the speckle pattern does still remain.

A set of clinical images are used in evaluation. A total of 500 frames are used to evaluate filtering performance, taken from 100 videos from 40 patients. They were scanned using a General Electric Vivid 7 Series scanner (GE Healthcare, Piscataway, NJ, USA). The results of applying the filters to the image of Fig. 1(a) are shown in Fig. 5.

The local statistics filters output are quite similar in appearance, and still contain some speckle. As with the simulated images, the anisotropic diffusion filters produce output with a range of characteristics. The PMAD filter produces images which are extremely blurred. The SRAD and DPAD filters both show strong speckle suppression, however the SRAD output appears more distorted. As with the simulated images, the CED and NCD filters introduce small scale artefacts to the images. The OSRAD filter again shows strong speckle suppression. Frames processed with the Zong wavelet filter have a somewhat washed-out appearance, and not all of the speckle is removed. The GLM, NMWD and Geometric filtered frames have most of the speckle removed, however the GLM output appears slightly blurred.

Five image quality metrics are applied to both the simulated and clinical echocardiographic images. In addition to the FoM and the edge MSE are detailed above, the following are considered:

Structural Similarity (SSIM) The SSIM measure (Wang et al., 2004) to asses the preservation of structural information in the filtering process:

$$SSIM = \frac{1}{M} \sum \frac{(2\mu_1\mu_2 + C_1)(2\sigma_{12} + C_2)}{(\mu_1^2 + \mu_2^2 + C_1)(\sigma_1^2 + \sigma_2^2 + C_2)} \tag{26}$$

where μ_1, μ_2 and σ_1, σ_2 are the means and standard deviations of the images being compared, and σ_{12} is the covariance between them. These quantities are calculated using local statistics within a total of M windows, the average of which is taken in (26). Constants $C_1, C_2 \ll 1$ ensure stability (Wang et al., 2004), and M is chosen as 32. The SSIM has values in the $0 \rightarrow 1$ range, with unity representing structurally identical images.

Contrast to Noise Ratio (CNR) The CNR quantifies the level of contrast between a region of interest and the background, and is calculated as:

$$CNR = \frac{|\mu_1 - \mu_2|}{\sqrt{\sigma_1^2 + \sigma_2^2}} \tag{27}$$

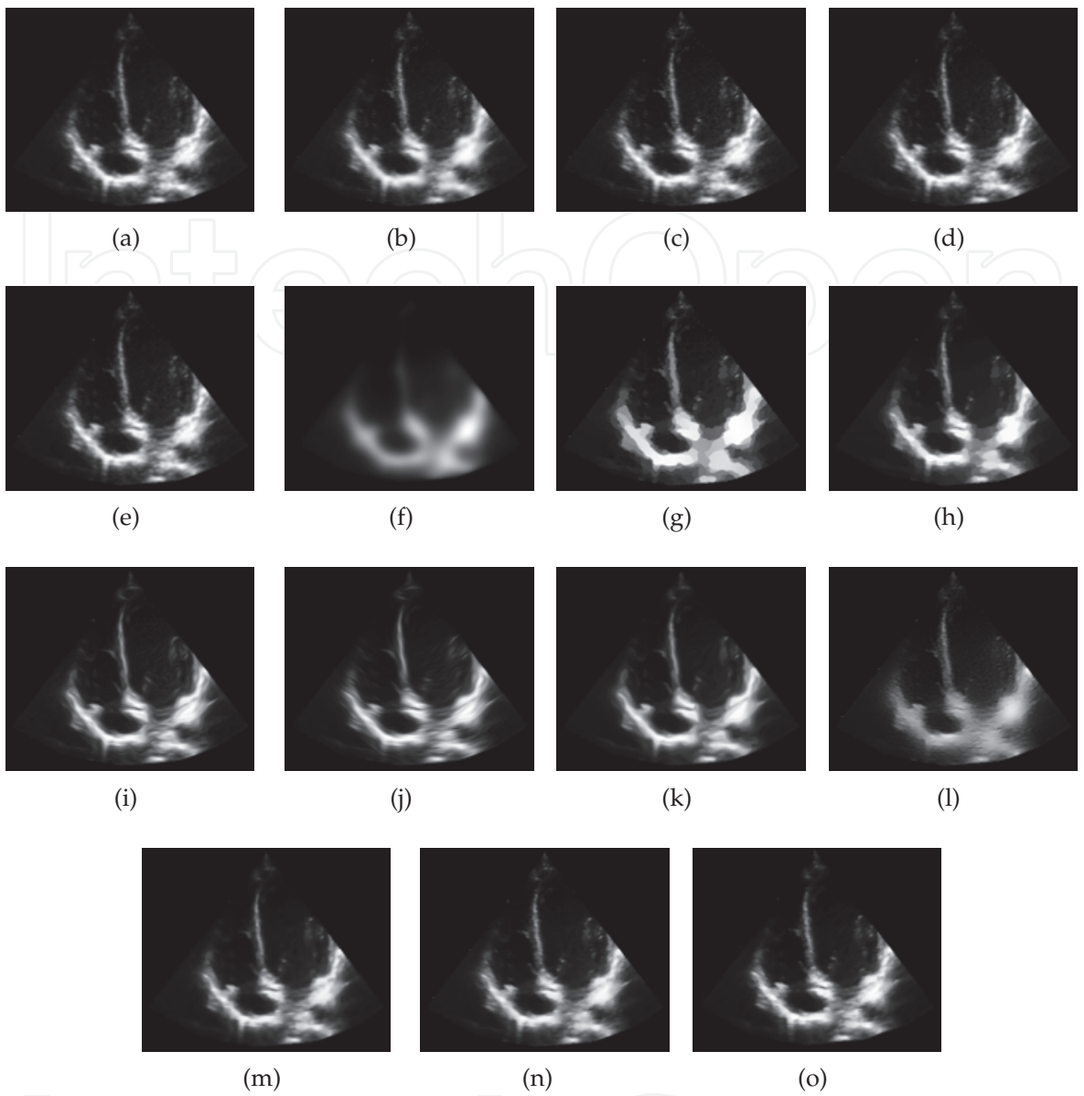

Fig. 5. Speckle filter output for the clinical image of Fig. 1(a). (a) Lee, (b) Kuan, (c) Frost, (d) EnhLee, (e) EnhFrost, (f) PMAD, (g) SRAD, (h) DPAD, (i) CED, (j) NCD, (k) OSRAD, (l) Zong, (m) GLM, (n) NMWD, (o) Geo.

where μ_1 and σ_1^2 are the mean and variance of a region of interest, and μ_2 and σ_2^2 are the mean and variance of a similar sized region in the image background.

SNR$_\mathbf{A}$ Burckhardt's (Burckhardt, 1978) SNR_A quantifies the level of speckle as the ratio of mean to standard deviation of the amplitude values.

For the simulated images, the SNR_A metric shows that the level of speckle is reduced by all of the filters. The MW reference has a higher average SNR_A than the post processing filters as expected, although some post processing filters exceed or match the MW SNR_A in individual regions. The NMWD and OSRAD filters achieve the highest average SNR_A values of the speckle reduction filters. The SRAD filter also performs well in this measure of speckle

reduction. The OSRAD filter exceeds the average SNR_A of the MW reference in one image region, and matches it in another. SRAD exceeds the MW reference average SNR_A in a single image region. The rest of the anisotropic diffusion methods have varying results as quantified by SNR_A. The NCD, DPAD and PMAD filters are rated highly, however the CED method performs poorly. Of the SAR filters, the Lee filter achieves the highest SNR_A score. Apart from the NMWD filter, the wavelet based methods perform quite poorly in this test.

Application of the other image quality metrics to the simulated images shows that the OSRAD, CED and NCD filters have the lowest edge region MSE, i.e. the smallest difference in the intensity of pixels close to image edges. By contrast, the FoM metric quantifies the average distortion in edge pixel locations between each filtered image and the MW reference image. The filters which perform best here are the Zong wavelet filter and the SAR filters. The filters with output most similar to the MW edges, as measured by the edge region MSE, perform poorly in the FoM. The SSIM metric compares the average structural similarity of filtered output with the MW reference. Calculated values are quite low, with the CED filter having the highest average of 0.22. Thus the speckle filters output are not structurally similar to the MW reference images. The CNR metric quantifies the average difference in contrast between each filtered output and the corresponding MW reference. Negative CNR values here indicate a lower contrast value than the MW reference. Over one third of the filters show improved average contrast relative to the MW image, the greatest of which are for the PMAD and OSRAD filters.

Applying metrics to the output of the clinical image set shows that the filters which remove the most speckle are the same as in the simulated case, although the level of improvement in the SNR_A metric is lower than for the simulated images. The smaller SNR_A increase can be explained by the differences in image content between the simulated and clinical images. Unlike the simulated images, the clinical images contain specular as well as scattered reflections. In addition they contain deviations from Rayleigh statistics (Molthen et al., 1995). The OSRAD filter achieves the highest average FoM value. The diffusion filters in general achieve mixed FoM scores, while some of the SAR filters achieve quite high scores. The Enhanced Lee, Frost and Zong filters are on average the most similar to the speckled input according to the SSIM metric. For the Enhanced Lee and Frost filters, the SNR_A values indicate that this may be due to a low level of overall filtering. The CNR shows that the contrast increases for all post processing filters, with the OSRAD, SRAD and NMWD attaining the greatest improvement. The lowest average difference in edge region pixel intensity due to filtering is observed for the NMWD and OSRAD filters. The Frost, CED and Kuan filters also preserve the content of edge region pixels quite well as measured by this metric.

The computational requirements for each of the filtering methods are determined by calculation of the number of multiplications, additions, and look-up table operations. A number of considerations are detailed here. For the anisotropic diffusion filters, the choice of discretization method has a large impact on computational requirements. A discretization scheme which allows the choice of a larger timestep (τ) can achieve a given level of diffusion with less iterations. Three discretization methods were compared: a simple explicit scheme, the Additive Operator Splitting (AOS) scheme of (Weickert et al., 1998), and the Jacobi scheme of (Krissian et al., 2007). For each of these methods the error is found relative to a reference diffusion (explicit discretization with a very small τ) for the diffusion methods of (Perona & Malik, 1990) and (Aja-Fernandez & Alberola-Lopez, 2006). The error for all

discretisation schemes increases with larger τ. The error measured for the explicit scheme is small as expected, but the valid range of τ is constrained to small values. The error for the AOS scheme and the Jacobi method are higher than the explicit method. It is observed that the AOS scheme performs similarly for both the PMAD and DPAD diffusion methods, while the Jacobi discretization results in a significantly higher error for one of the diffusion functions. Further details can be found in (Finn et al., 2010). In the analysis of computational requirements, various other implementational details are considered, which are also detailed in this paper.

After quantification of the filter complexity for each filter, it was found that the most computationally intensive method is the NMWD filter, for typical filtering scenarios. This filter required almost five times as many multiplications as the next most demanding. The DPAD and SRAD filters have higher requirements than the other diffusion methods, but this is due to the large number of iterations required. The DWT used in the GLM filter requires much more computation than the DWT of the Zong filter. The efficiency of the semi-implicit scheme for the anisotropic diffusion filters is demonstrated by the similarity between their requirements and the SAR filters.

The use of simulated images permits comparison of speckle reduced filtered output with a maximally noise free reference. Quantification of speckle reduction capabilities using the SNR_A has shown that anisotropic diffusion based methods have in general the strongest suppression of speckle. The application of objective metrics such as the FoM, Edge MSE, CNR and SSIM quantifies other aspects of the filtering process. The improvement in CNR values of the SRAD, OSRAD and NMWD filters shows that these methods can achieve greater contrast than other methods.. Average edge pixel distortion due to filtering was lowest in the matrix diffusion and SAR filters, as seen by both the high FoM and low edge region MSE values. This indicates that these methods distort image boundaries the least amount. In the case of the SAR filters however, this is due to a low overall level of filtering.

Based on analysis of computational complexity, it is clear that there is a large disparity in the requirements of the speckle reduction methods considered here. The SAR and geometric filters have the lowest computational overhead, but this comes at the expense of lower speckle reduction capability. The wavelet based approaches are hindered from a performance perspective by the requirements of implementing wavelet analysis and reconstruction. In particular, the NMWD filter performs wavelet analysis and reconstruction for each iteration, leading to the largest requirement of all considered methods. The anisotropic diffusion methods all have similar processing needs, and these fall between those of the SAR methods and the wavelet based filters. Efficient implementation of these methods is only possible by the use of a discretisation method which allows a large timestep.

This study concluded by noting that the optimal filtering method for echocardiography depends on the scenario: If the main concern is a constraint on available processing capability, the SAR filters are the best due to their low requirements. In particular the Lee filter is a reasonable choice given its speckle suppression ability and low overhead. If however the main objective is to remove as much speckle as possible, the NMWD filter has the strongest speckle suppression capabilities. This comes at the expense of the highest computational complexity however, and the preservation of edges is not optimal. The OSRAD method represents the best trade-off between both of these situations. The level of speckle suppression achievable

using this approach is very close to that of the NMWD, with the advantage of a much smaller processing overhead. The OSRAD method was therefore considered the best compromise.

5. Conclusion

This chapter has presented an overview of the speckle artefact from ultrasound, with a focus on echocardiography. A description of nature and modelling of speckle was presented. The reduction or removal of speckle from clinical ultrasound and echocardiography is a common goal of image processing in the literature, and many of the recent approaches are detailed in Section 3 above.

The assessment of the quality of speckle reduced video is not a straightforward task. In the literature, many methods of review focus on numerical metrics and visual analysis without consideration of clinical opinion. For the case of clinical echocardiography, the extension of assessment technique to include expert physician opinion allows a more realistic evaluation. Image quality metrics are still of high importance however, due to their ease of computation and their objective nature.

This chapter has described a study in which the relationships between such metrics and objective expert opinion are explored, and it was found that certain metrics are strong indicators of physicians assessment. An extensive study of a large number of speckle reduction filters is also described above, focusing on real world application. A large number of speckled images, both clinical and simulated, are used as test data. Assessment includes image quality metrics (some of which are indicators of physicians evaluation) and also a computational requirement analysis.

An important aspect of evaluating the quality of speckle reduced echocardiography is that there are often differences between clinical and image processing perspectives. In particular, clinical experts do not appear to prefer the use of speckle filtered images for diagnostic analysis. It should be noted that there are situations where speckle preservation is desired. In particular, clinicians may prefer the original speckled images in some situations (Zhang et al., 2007). Dantas and Costa (Dantas & Costa, 2007) noted that when speckle is removed, the loss of false fine detail can lead to a perceived reduction in image sharpness, even if the boundaries of anatomical structures are not blurred. The speckle pattern is seen as having diagnostic utility in specific conditions, such as diffuse liver diseases (Kadah et al., 1996) in abdominal imaging and hypertrophic cardiomyopathy in echocardiography (Massay et al., 1989). Some automated processing tasks take advantage of the speckle pattern, such as feature tracking (Trahey et al., 1987) and tissue characterisation, some recent examples of which can be found in (De Marchi et al., 2006; Maurice et al., 2005; Tsui et al., 2005). So while some particular applications are best served by preserving speckle, others benefit from its removal. Perhaps the most pragmatic approach was taken by Zhang *et al.* (Zhang et al., 2007), who promote the idea of the speckle reduced image as a complementary addition to the original image, rather than a replacement.

6. References

Abd-Elmoniem, K., Youssef, A.-B. & Kadah, Y. (2002). Real-time speckle reduction and coherence enhancement in ultrasound imaging via nonlinear anisotropic diffusion,

49(9): 997–1014.
Achim, A., Bezerianos, A. & Tsakalides, P. (2001). Novel Bayesian multiscale method for speckle removal in medical ultrasound images, 20(8): 772–783.
Adam, D., Beilin-Nissan, S., Friedman, Z. & Behar, V. (2006). The combined effect of spatial compounding and nonlinear filtering on the speckle reduction in ultrasound images, *Ultrasonics* 44(2): 166–181.
Adelson, E., Anderson, C., Bergen, J., Burt, P. & Ogden, J. (1984). Pyramid methods in image processing, *RCA Engineer* 29(6).
Aiazzi, B., Alparone, L. & Baronti, S. (1998). Multiresolution local-statistics speckle filtering based on a ratio Laplacian pyramid, 36(5): 1466–1476.
Aja-Fernandez, S. & Alberola-Lopez, C. (2006). On the estimation of the coefficient of variation for anisotropic diffusion speckle filtering, 15(9): 2694–2701.
Bamber, J. C. & Daft, C. (1986). Adaptive filtering for reduction of speckle in ultrasonic pulse-echo images., *Ultrasonics* pp. 41–44.
Bamber, J. & Phelps, J. (1991). Real-time implementation of coherent speckle suppression in B-scan images, *Ultrasonics* 29(3): 218–224.
Behar, V., Adam, D. & Friedman, Z. (2003). A new method of spatial compounding imaging, *Ultrasonics* 41(5): 377–384.
Burckhardt, C. (1978). Speckle in ultrasound B-Mode scans, 25(1): 1–6.
Burt, P. & Adelson, E. (1983). The Laplacian pyramid as a compact image code, 31(4): 532–540.
Catté, F., Lions, P.-L., Morel, J.-M. & Coll, T. (1992). Image selective smoothing and edge detection by nonlinear diffusion, *SIAM J. Numer. Anal.* 29(1): 182–193.
Chen, Y., Yin, R., Flynn, P. & Broschat, S. (2003). Aggressive region growing for speckle reduction in ultrasound images, *Pattern Recogn. Lett.* 24(4-5): 677–691.
Coupé, P., Hellier, P., Kervrann, C. & Barillot, C. (2009). Nonlocal means-based speckle filtering for ultrasound images, 18(10): 2221–2229.
Crimmins, T. (1985). Geometric filter for speckle reduction, *Appl. Opt.* 24: 1438–1443.
Dantas, R. & Costa, E. (2007). Ultrasound speckle reduction using modified Gabor filters, 54(3): 530–538.
Dantas, R. G., Costa, E. T. & Leeman, S. (2005). Ultrasound speckle and equivalent scatterers, *Ultrasonics* 43(6): 405–420.
De Marchi, L., Testoni, N. & Speciale, N. (2006). Prostate tissue characterization via ultrasound speckle statistics, *IEEE Int. Symp. Signal Processing Information Technology*, pp. 208–211.
Dempster, A. P., Laird, N. M. & Rubin, D. B. (1977). Maximum likelihood from incomplete data via the EM algorithm, *J. R. Stat. Soc. B* 39(1): 1–38.
Donoho, D. L. (1995). De-noising by soft-thresholding, 41(3): 613–627.
Finn, S., Glavin, M. & Jones, E. (2010). Echocardiographic speckle reduction comparison, 58(1): 82–101.
Finn, S., Jones, E. & Glavin, M. (2009). Objective and subjective evaluations of quality for speckle reduced echocardiography, *Proc. IEEE Intl. Annu. Conf. Engineering Medicine and Biology Society*, pp. 503–506.
Frost, V. S., Stiles, J. A., Shanmugan, K. S. & Holtzman, J. C. (1982). A model for radar images and its application to adaptive digital filtering of multiplicative noise, 4(2): 157–166.
Fu, X.-W., Ding, M.-Y. & Cai, C. (2010). Despeckling of medical ultrasound images based on quantum-inspired adaptive threshold, *Electron. Lett.* 46(13): 889–891.

Galloway, R. L., McDermott, B. A. & Thurstone, F. L. (1988). A frequency diversity process for speckle reduction in real-time ultrasonic images, pp. 45–49.

Gehlbach, S. M. & Sommer, F. G. (1987). Frequency diversity speckle processing, *Ultrasonic Imaging* 9: 92–105.

Goodman, J. (1975). Statistical properties of laser speckle patterns, *in* J. Dainty (ed.), *Laser Speckle and Related Phenomena*, Vol. 9 of *Topics in Applied Physics*, Springer, Berlin, pp. 9–75.

Goodman, J. W. (1976). Some fundamental properties of speckle, *J. Opt. Soc. Am.* 66(11): 1145–1150.

Guo, H., Odegard, J., Lang, M., Gopinath, R., Selesnick, I. & Burrus, C. (1994). Wavelet based speckle reduction with application to SAR based ATD/R, *Proc. IEEE Int. Conf. Image Processing*, Vol. 1, pp. 75–79.

Gupta, N., Swamy, M. & Plotkin, E. (2005). Despeckling of medical ultrasound images using data and rate adaptive lossy compression, 24(6): 743–754.

Hao, X., Gao, S. & Gao, X. (1999). A novel multiscale nonlinear thresholding method for ultrasonic speckle suppressing, 18(9): 787–794.

Huang, H.-C., Chen, J.-Y., Wang, S.-D. & Chen, C.-M. (2003). Adaptive ultrasonic speckle reduction based on the slope-facet model, *Ultrasound Med. Biol.* 29(8): 1161–1175.

Jensen, J. (1991). A model for the propagation and scattering of ultrasound in tissue, *J. Acoust. Soc. Am.* 89: 182–190.

Jensen, J. A. (1996). FIELD: A program for simulating ultrasound systems, *Proc. 10th NordicBaltic Conference Biomedical Imaging*, Vol. 4, pp. 351–353.

Jespersen, S., Wilhjelm, J. & Sillesen, H. (2000). In vitro spatial compound scanning for improved visualization of atherosclerosis, *Ultrasound Med. Biol.* 26(8): 1357–1362.

Kadah, Y., Farag, A., Zurada, J., Badawi, A. & Youssef, A.-B. (1996). Classification algorithms for quantitative tissue characterization of diffuse liver disease from ultrasound images, 15(4): 466–478.

Karaman, M., Kutay, M. & Bozdagi, G. (1995). An adaptive speckle suppression filter for medical ultrasonic imaging, 14(2): 283–292.

Koo, J. I. & Park, S. B. (1991). Speckle reduction with edge preservation in medical ultrasonic images using a homogeneous region growing mean filter (HRGMF), *Ultrasonic Imaging* 13(3): 211–237.

Krissian, K. (2002). Flux-based anisotropic diffusion applied to enhancement of 3-d angiogram, 21(11): 1440–1442.

Krissian, K., Westin, C.-F., Kikinis, R. & Vosburgh, K. (2007). Oriented speckle reducing anisotropic diffusion, 16(5): 1412–1424.

Kruskal, W. H. & Wallis, W. A. (1953). Errata: Use of ranks in one-criterion variance analysis, *J. Am. Stat. Assoc.* 48(264): 907–911.

Kuan, D., Sawchuk, A., Strand, T. & Chavel, P. (1987). Adaptive restoration of images with speckle, ASSP-35(3): 373–383.

Lee, J.-S. (1980). Digital image enhancement and noise filtering by use of local statistics, PAMI-2(2): 165–168.

Lee, J.-S. (1981). Speckle analysis and smoothing of synthetic aperture radar images, *Comput. Vision Graph.* 17(1): 24–32.

Lizzi, F. L., Astor, M., Liu, T., Deng, C., Coleman, D. J. & Silverman, R. H. (1997). Ultrasonic spectrum analysis for tissue assays and therapy evaluation, *Int. J. Imag. Syst. Tech.* 8(1): 3–10.

Loizou, C. P., Pattichis, C. S., Christodoulou, C. I., Istepanian, R. S. H., Pantziaris, M. & Nicolaides, A. (2005). Comparative evaluation of despeckle filtering in ultrasound imaging of the carotid artery, 52(10): 1653–1669.

Lopes, A., Touzi, R. & Nezry, E. (1990). Adaptive speckle filters and scene heterogeneity, 28(6): 992–1000.

Loupas, T., McDicken, W. & Allan, P. (1989). An adaptive weighted median filter for speckle suppression in medical ultrasonic images, 36(1): 129 –135.

Magnin, P. A., von Ramm, O. T. & Thurstone, F. L. (1982). Frequency compounding for speckle contrast reduction in phased array images, *Ultrasonic Imaging* 4: 267–281.

Mallat, S. & Zhong, S. (1992). Characterization of signals from multiscale edges, 14(7): 710–732.

Massay, R. J., Logan-Sinclair, R. B., Bamber, J. C. & Gibson, D. G. (1989). Quantitative effects of speckle reduction on cross sectional echocardiographic images., *Br. Heart J.* 62(4): 298–304.

Mateo, J. L. & Fernández-Caballero, A. (2009). Finding out general tendencies in speckle noise reduction in ultrasound images, *Expert Syst. Appl.* 36(4): 7786–7797.

Maurice, R. L., Brusseau, E., Finet, G. & Cloutier, G. (2005). On the potential of the Lagrangian speckle model estimator to characterize atherosclerotic plaques in endovascular elastography: In vitro experiments using an excised human carotid artery, *Ultrasound Med. Biol.* 31(1): 85–91.

Michailovich, O. & Adam, D. (2005). A novel approach to the 2-d blind deconvolution problem in medical ultrasound, 24(1): 86–104.

Middleton, W. D. & Kurtz, A. B. (2004). *Ultrasound: The Requisites (Requisites in Radiology Series)*, 2 edn, Elsevier Mosby, Philadelphia, PA.

Molthen, R. C., Shankar, P. M. & Reid, J. M. (1995). Characterization of ultrasonic B-scans using non-Rayleigh statistics, *Ultrasound Med. Biol.* 21(2): 161–170.

Moulin, P. (1993). A wavelet regularization method for diffuse radar-target imaging and speckle-noise reduction, 3(1): 123–134.

Newhouse, V., Bilgutay, N., Saniie, J. & Furgason, E. (1982). Flaw-to-grain echo enhancement by split-spectrum processing, *Ultrasonics* 20(2): 59–68.

Ng, J., Prager, R., Kingsbury, N., Treece, G. & Gee, A. (2006). Modeling ultrasound imaging as a linear, shift-variant system, 53(3): 549–563.

Ng, J., Prager, R., Kingsbury, N., Treece, G. & Gee, A. (2007). Wavelet restoration of medical pulse-echo ultrasound images in an em framework, 54(3): 550–568.

O'Donnell, M. & Silverstein, S. (1988). Optimum displacement for compound image generation in medical ultrasound, 35(4): 470–476.

Pai-Chi, L. & O'Donnell, M. (1994). Elevational spatial compounding, *Ultrasonic imaging* 16(3): 176–189.

Perona, P. & Malik, J. (1990). Scale-space and edge detection using anisotropic diffusion, 12(7): 629–639.

Pižurica, A., Philips, W., Lemahieu, I. & Acheroy, M. (2003). A versatile wavelet domain noise filtration technique for medical imaging, 22(3): 323–331.

Pratt, W. K. (1977). *Digital Signal Processing*, Wiley, New York.

Quistgaard, J. (1997). Signal acquisition and processing in medical diagnostic ultrasound, 14(1): 67–74.

Rabbani, H., Vafadust, M., Abolmaesumi, P. & Gazor, S. (2008). Speckle noise reduction of medical ultrasound images in complex wavelet domain using mixture priors, 55(9): 2152–2160.

Rumack, C., Wilson, S., Charboneau, J. & Johnson, J. (2004). *Diagnostic ultrasound*, 3rd edn, Elsevier Mosby, Philadelphia, PA.

Sattar, F., Floreby, L., Salomonsson, G. & Lovstrom, B. (1997). Image enhancement based on a nonlinear multiscale method, 6(6): 888–895.

Shankar, P., Dumane, V., Reid, J., Genis, V., Forsberg, F., Piccoli, C. & Goldberg, B. (2001). Classification of ultrasonic b-mode images of breast masses using nakagami distribution, 48(2): 569–580.

Shankar, P. M. (1995). A model for ultrasonic scattering from tissues based on the K distribution, *Phys. Med. Biol.* 40(10): 1633–1649.

Smolíováí, R., Wachowiak, M. P. & Zurada, J. M. (2004). An information-theoretic approach to estimating ultrasound backscatter characteristics, *Comput. Biol. Med.* 34(4): 355–370.

Spearman, C. (1904). The proof and measurement of association between two things, *Amer. J. Psychol.* 15: 72–101.

Stetson, P., Sommer, F. & Macovski, A. (1997). Lesion contrast enhancement in medical ultrasound imaging, 16(4): 416–425.

Tay, P., Acton, S. & Hossack, J. (2006a). A stochastic approach to ultrasound despeckling, *Proc. 3rd IEEE Int. Symp. Biomedical Imaging: Nano to Macro*, pp. 221–224.

Tay, P., Acton, S. & Hossack, J. (2006b). Ultrasound despeckling using an adaptive window stochastic approach, *Proc. IEEE Int. Conf. Image Processing*, pp. 2549–2552.

Thakur, A. & Anand, R. (2005). Image quality based comparative evaluation of wavelet filters in ultrasound speckle reduction, *Digit. Signal Process.* 15(5): 455–465.

Thijssen, J. M. (2003). Ultrasonic speckle formation, analysis and processing applied to tissue characterization, *Pattern Recogn. Lett.* 24(4-5): 659–675.

Trahey, G. E., Allison, J. W., Smith, S. W. & von Ramm, O. T. (1986). A quantitative approach to speckle reduction via frequency compounding, *Ultrasonic Imaging* 8: 151–164.

Trahey, G. E., Allison, J. W. & von Ramm, O. T. (1987). Angle independent ultrasonic detection of blood flow, BME-34(12): 965–967.

Trahey, G. E., Smith, S. W. & von Ramm, O. T. (1986). Speckle reduction in medical ultrasound via spatial compounding, *Proc. SPIE Medicine XIV PACS*, Vol. 4, pp. 629–637.

Tsui, P.-H., Wang, S.-H. & Huang, C.-C. (2005). The effect of logarithmic compression on estimation of the nakagami parameter for ultrasonic tissue characterization: a simulation study, *Phys. Med. Biol.* 50(14): 3235–3244.

Wagner, R., Insana, M. & Smith, S. (1988). Fundamental correlation lengths of coherent speckle in medical ultrasonic images, 35(1): 34–44.

Wagner, R., Smith, S., Sandrik, J. & Lopez, H. (1983). Statistics of Speckle in Ultrasound B-Scans, 30(3): 156–163.

Wang, Z., Bovik, A., Sheikh, H. & Simoncelli, E. (2004). Image quality assessment: from error visibility to structural similarity, 13(4): 600–612.

Weickert, J. (1998). *Anisotropic Diffusion in Image Processing*, Teubner-Verlag, Stuttgart, Germany. Out of print.

Weickert, J. (1999). Coherence-enhancing diffusion filtering, *Int. J. Comput. Vision* 31(2-3): 111–127.

Weickert, J., Romeny, B. & Viergever, M. (1998). Efficient and reliable schemes for nonlinear diffusion filtering, 7(3): 398–410.

Yu, Y. & Acton, S. (2002). Speckle reducing anisotropic diffusion, 11(11): 1260–1270.

Yu, Y. & Acton, S. (2004). Edge detection in ultrasound imagery using the instantaneous coefficient of variation, 13(12): 1640–1655.

Yue, Y., Croitoru, M., Bidani, A., Zwischenberger, J. & Clark, J. J. (2006). Nonlinear multiscale wavelet diffusion for speckle suppression and edge enhancement in ultrasound images, 25(3): 297–311.

Zhang, F., Yoo, Y. M., Koh, L. M. & Kim, Y. (2007). Nonlinear diffusion in Laplacian pyramid domain for ultrasonic speckle reduction, 26(2): 200–211.

Zong, X., Laine, A. & Geiser, E. (1998). Speckle reduction and contrast enhancement of echocardiograms via multiscale nonlinear processing, 17(4): 532–540.

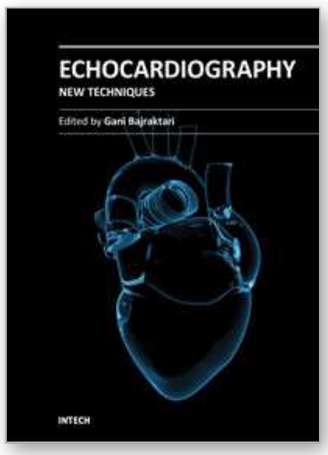

Echocardiography - New Techniques

Edited by Prof. Gani Bajraktari

ISBN 978-953-307-762-8
Hard cover, 218 pages
Publisher InTech
Published online 18, January, 2012
Published in print edition January, 2012

The book "Echocardiography - New Techniques" brings worldwide contributions from highly acclaimed clinical and imaging science investigators, and representatives from academic medical centers. Each chapter is designed and written to be accessible to those with a basic knowledge of echocardiography. Additionally, the chapters are meant to be stimulating and educational to the experts and investigators in the field of echocardiography. This book is aimed primarily at cardiology fellows on their basic echocardiography rotation, fellows in general internal medicine, radiology and emergency medicine, and experts in the arena of echocardiography. Over the last few decades, the rate of technological advancements has developed dramatically, resulting in new techniques and improved echocardiographic imaging. The authors of this book focused on presenting the most advanced techniques useful in today's research and in daily clinical practice. These advanced techniques are utilized in the detection of different cardiac pathologies in patients, in contributing to their clinical decision, as well as follow-up and outcome predictions. In addition to the advanced techniques covered, this book expounds upon several special pathologies with respect to the functions of echocardiography.

How to reference

In order to correctly reference this scholarly work, feel free to copy and paste the following:

Seán Finn, Martin Glavin and Edward Jones (2012). Speckle Reduction in Echocardiography: Trends and Perceptions, Echocardiography - New Techniques, Prof. Gani Bajraktari (Ed.), ISBN: 978-953-307-762-8, InTech, Available from: http://www.intechopen.com/books/echocardiography-new-techniques/speckle-reduction-in-echocardiography-trends-and-perceptions

INTECH
open science | open minds

InTech Europe
University Campus STeP Ri
Slavka Krautzeka 83/A
51000 Rijeka, Croatia
Phone: +385 (51) 770 447
Fax: +385 (51) 686 166
www.intechopen.com

InTech China
Unit 405, Office Block, Hotel Equatorial Shanghai
No.65, Yan An Road (West), Shanghai, 200040, China
中国上海市延安西路65号上海国际贵都大饭店办公楼405单元
Phone: +86-21-62489820
Fax: +86-21-62489821

IntechOpen